Implementing the Locally-Corrected Nyström Method

Stephen D. Gedney
Department of Electrical and Computer Engineering
University of Kentucky
Lexington, KY 40506-0046

I. Introduction

The focus of this tutorial is to detail the implementation of a locally corrected Nyström (LCN) based solution of three-dimensional electromagnetic scattering problems. The LCN method has demonstrated exponentially convergent solutions for electromagnetic scattering problems, including problems involving PEC scatterers [1, 2], dielectric scatterers using surface [3] and volume integral equation methods [4], as well as for thin-wire antennas [5]. The principal advantages of employing a methodology that is high-order convergent are: *i*) the computer resources required to realize accuracy to a desired tolerance can be greatly reduced as compared to a classical low-order technique, *ii*) accurate estimations of the solution error can be efficiently obtained, and *iii*) the LCN method is quite simple to implement. As the LCN method is maturing it is being applied to more practical engineering design problems and is proving to be a very powerful solution technique.

The following sections of this tutorial are aimed at outlining more specific details of implementing the LCN method. While space limits a full description of all aspects of an implementation, it is hoped that enough detail is provided to encourage readers to implement and test this very powerful solution technique.

II. Integral Equations

Consider the interaction of a time-harmonic electromagnetic wave ($e^{j\omega t}$ time-dependence) with a material scatterer made of a composite of penetrable materials (with piecewise constant material profiles) and non-penetrable conductors. Let the i^{th} region with material profile (ε_i, μ_i) be defined as volume V_i. A surface separating volumes V_i and V_j is denoted as $S_{i,j}$. Let $S_{i,j}^+$ denote the surface just inside V_i, and $S_{i,j}^-$ denote the surface just inside V_j. Equivalent current densities are then placed on surfaces separating each material volume. These are defined as:

$$\vec{J}_{i,j}^{+} = \hat{n}_i \times \vec{H}\Big|_{S_{i,j}^+}, \quad \vec{M}_{i,j}^{+} = -\hat{n}_i \times \vec{E}\Big|_{S_{i,j}^+}, \quad \vec{J}_{i,j}^{-} = \hat{n}_j \times \vec{H}\Big|_{S_{i,j}^-}, \quad \vec{M}_{i,j}^{-} = -\hat{n}_j \times \vec{E}\Big|_{S_{i,j}^-}, \tag{1}$$

where $\hat{n}_i$ and $\hat{n}_j$ are the unit normal directed into V_i and V_j, respectively. At any point on $S_{i,j}$ $\hat{n}_j = -\hat{n}_i$, and the tangential fields are continuous, thus:

$$\vec{J}_{i,j}^{+} = -\vec{J}_{i,j}^{-} = \vec{J}_{i,j}, \quad \vec{M}_{i,j}^{+} = -\vec{M}_{i,j}^{-} = \vec{M}_{i,j}. \tag{2}$$

On the surface of a perfect conductor, only the electric current density is supported. Thus,

$$\vec{J}_{i,p} = \hat{n}_i \times \vec{H}\Big|_{S_{i,p}^{+}}. \tag{3}$$

The scattered electric and magnetic fields radiated by the equivalent currents in volume V_i are computed as:

$$\vec{E}_i^{scat}\left(\vec{J}_{eq}, \vec{M}_{eq}\right) = \eta_i \mathbf{L}_i\left(\vec{J}_{eq}\right) - \mathbf{K}_i\left(\vec{M}_{eq}\right), \tag{4}$$

$$\vec{H}_i^{scat}\left(\vec{J}_{eq}, \vec{M}_{eq}\right) = \mathbf{K}_i\left(\vec{J}_{eq}\right) + \eta_i^{-1} \mathbf{L}_i\left(\vec{M}_{eq}\right), \tag{5}$$

where

$$\mathbf{L}_i\left(\vec{X}_{eq}\right) = -jk_i \int_{\Omega} \left[\overline{\overline{I}} + \frac{1}{k_i^2}\nabla\nabla\right] \cdot \vec{X}_{eq}\left(\vec{r}'\right) G_i\left(\vec{r}, \vec{r}'\right) d\Omega', \tag{6}$$

$$\mathbf{K}_i\left(\vec{X}_{eq}\right) = \int_{\Omega} \nabla G_i\left(\vec{r}, \vec{r}'\right) \times \vec{X}_{eq}\left(\vec{r}'\right) d\Omega', \tag{7}$$

and Ω is either a surface or volume, $\overline{\overline{I}}$ is the unit dyad, $G_i\left(\vec{r}, \vec{r}'\right) = e^{-jk_i|\vec{r}-\vec{r}'|}/4\pi|\vec{r}-\vec{r}'|$, $k_i = \omega\sqrt{\varepsilon_i \mu_i}$ and $\eta_i = \sqrt{\mu_i/\varepsilon_i}$.

A surface integral formulation is then derived by enforcing the appropriate constraints on each material boundary. A combined field formulation based on Müller's formulation [6, 7] is applied on material surfaces leading to:

$$\vec{t} \cdot \varepsilon_{r_i} \vec{E}_i^{inc}\Big|_{S_{i,j}^{+}} + \vec{t} \cdot \varepsilon_{r_j} \vec{E}_j^{inc}\Big|_{S_{i,j}^{-}} = \vec{t} \cdot \hat{n}_i \times \vec{M}_{i,j}\left(\varepsilon_{r_i} + \varepsilon_{r_j}\right) - \vec{t}\,\varepsilon_{r_i} \vec{E}_i^{scat}\Big|_{S_{i,j}^{+}} - \vec{t} \cdot \varepsilon_{r_j} \vec{E}_j^{scat}\Big|_{S_{i,j}^{-}}, \tag{8}$$

$$\vec{t} \cdot \mu_{r_i} \vec{H}^{inc}\Big|_{S_{i,j}^{+}} + \vec{t} \cdot \mu_{r_j} \vec{H}^{inc}\Big|_{S_{i,j}^{-}} = -\vec{t} \cdot \hat{n}_i \times \vec{J}_{i,j}\left(\mu_{r_i} + \mu_{r_j}\right) - \vec{t} \cdot \mu_{r_i} \vec{H}^{scat}\Big|_{S_{i,j}^{+}} - \vec{t} \cdot \mu_{r_j} \vec{H}^{scat}\Big|_{S_{i,j}^{-}}, \tag{9}$$

where, $\vec{E}_i^{inc}$, $\vec{H}_i^{inc}$ are radiated by impressed sources in region *i*, $\vec{E}_i^{scat}$, $\vec{H}_i^{scat}$ are radiated by equivalent currents in volume V_i, and $\vec{t}$ is a test vector tangential to $S_{i,j}$. The advantage of this formulation over the classical PMCHWT (Poggio, Miller, Chang, Harrington, Wu and Tai) formulation [8] is that it behaves as a second-kind integral equation moderate to low contrast materials, and the hyper-singularity of the $\mathbf{L}$-operator in (6) is reduced by one order.

On a PEC surface, the combined field integral equation (CFIE) is applied [9]:

$$\frac{\alpha}{\eta_i} \vec{t} \cdot \vec{E}_i^{inc}\Big|_{S_{i,p}} + (1-\alpha)\vec{t} \cdot \hat{n} \times \vec{H}_i^{inc}\Big|_{S_{i,p}} = \frac{\alpha}{\eta_i}\left(-\vec{t} \cdot \vec{E}_i^{scat}\Big|_{S_{i,p}}\right) + (1-\alpha)\vec{t} \cdot \left(\vec{J}_{i,p} - \hat{n} \times \vec{H}_i^{scat}\Big|_{S_{i,p}}\right). \tag{10}$$

where α is a real constant, generally defined between 0 and 1.

III. Nyström Discretization

In [2], it was shown that the LCN method is equivalent to a moment method formulation with smooth basis and testing functions that employs a fixed-point numerical quadrature approximation for the outer integral. Through a simple transformation, this can identically be expressed as a quadrature-point matched method of moment formulation [10]. Then, mapping the currents to the quadrature points, the method of moment formulation can then be rendered in

an identical form as the LCN method [2]. Since most practitioners in computational electromagnetics (CEM) are trained in the method of moments, this paradigm will be followed in this tutorial.

It is assumed that the three-dimensional surfaces are discretized using high-order quadrilateral patches (Section IV). A set of basis functions is then introduced for each patch. For smooth surfaces, one can expand the vector surface current density in terms via Legendre polynomials [1, 2, 10] leading to a set of functions that is polynomial complete to order *p*:

$$\begin{aligned} \vec{J}_i^{\,j,k}\left(u^1,u^2\right) &= \vec{a}_i P_j\left(u^1\right) P_k\left(u^2\right)/\sqrt{g}, \\ \vec{M}_i^{\,j,k}\left(u^1,u^2\right) &= \vec{a}_i P_j\left(u^1\right) P_k\left(u^2\right)/\sqrt{g}, \end{aligned} \tag{11}$$

for $\left(i=1,2;\ \ j,k=0..p-1\right)$, where, following the notation of Stratton [11], (u^1,u^2) are the local curvilinear coordinates of the quadrilateral patch, $\vec{a}_i$ are the local unitary vectors and $\sqrt{g}$ is the Jacobian evaluated at (u^1,u^2), and $P_j(u)$ are j^{th}-order Legendre polynomials. Note that for simplicity, we have assumed identical basis orders along the u^1 and u^2 directions. In general, these do not have to be equal. Some observations are made for this choice of basis: 1) the basis functions are local to each quadrilateral patch and do not enforce current continuity across patch boundaries, 2) the *i*-th basis is directed along $\vec{a}_i$ and is tangential to the patch boundaries $u^j=0$ and $u^j=1$ ($j\neq i$), and 3) there are $2\times p^2$ basis functions per patch for each current type.

For geometries that lead to currents with known edge singularities (say a knife edge), basis functions with Jacobi polynomials can also be employed [2, 12]. Else, for general edge singularities, a mixed-order basis proposed by Çalişkan and Peterson can be employed [13, 14]. For the sake of this tutorial, we will limit the discussion to the polynomial complete basis in (11).

The currents in the integral operators in (8)-(10) are expanded via the basis functions in (11) and weighted by constant coefficients. This leads to $2\times p^2$ unknowns per patch for each current type. Consequently, $2\times p^2$ constraints must be enforced. To this end, an appropriate quadrature rule is introduced over each quadrilateral patch. For a quadrilateral patch, a convenient choice is the product of two *p*-point one-dimensional Gauss-Legendre quadrature rules [15]. This leads to p^2 abscissa points on the patch. Then, the integral operator is "tested" by performing the inner-dot product of the operator with a test vector at each of the quadrature abscissa points. A convenient choice for the test vector is simply the unitary vectors $\vec{a}_i$. On a material surface, the same testing procedure is used for the electric field integral equation (EFIE) and the magnetic field integral equation (MFIE) in (8) and (9), respectively. Thus, for each field type, there are a total of $2\times p^2$ constraints per patch. This leads to a square linear system of equations.

IV. High-Order Patch-Based Discretization

As found in [1, 2], the LCN method is most efficient when employing higher-order basis on large smooth curvilinear patches – that is, the error will converge to a desired accuracy with fewer unknowns. The reason for this is simple: higher-order basis converge more rapidly than lower order basis. Thus, with the LCN method it is desirable to model geometries with large curvilinear cells that represent the surface to sufficient accuracy. A balance of CPU time and memory is often realized with a discrete patch representation that has an average cell radius of

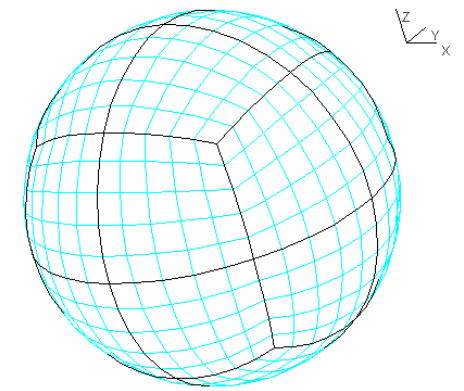

Fig. 1. Curvilinear quadrilateral cell discretization of a spherical surface with 24, 5th-order cells).

$\sim 1\ \lambda$. Thus, it becomes imperative to employ isoparametric curvilinear patches that accurately model a surface of arbitrary curvature. If one can not support such patches, then one is forced to use a refined discretization – thus losing the advantage of the high-order method. For classical low-order techniques, this has not been an issue since the slow convergence requires one to resolve the surface with a minimum of 10 to 20 edges per linear wavelength to get reasonable accuracy. Often, such fine sampling is also enough to represent a curved surface to sufficient accuracy using a piecewise linear approximation.

Most commercial mesh generation programs are limited by the order of curvilinear cells that can be generated. Most CAD packages provide at least bi-linear quadrilaterals (first order). Some will render bi-quadratic and very few will render up to bi-cubic elements. This is still too limiting, since arbitrary order is desirable for a high-order method. To have this ability, we have developed a mesh tool that will generate quadrilateral elements of arbitrary order from an initial coarse linear discretization. As an example, Fig. 1 illustrates a sphere that is approximated by 24 fifth-order quadrilateral patches that was generated by our mesh tool.

A quadrilateral patch of order *n* is represented by $(n+1)\times(n+1)$ nodes that lie on the surface. In the unitary space, these nodes are uniformly spaced, as illustrated in Fig. 2. Each node has a physical coordinate $\vec{r}_{j,k}$ ($j,k=0,n$). The position at any arbitrary coordinate (u^1,u^2) can be obtained via interpolation:

$$\vec{r}(u^1,u^2)=\sum_{k=0}^{n}\sum_{j=0}^{n}\Phi_j^n\left(u^1\right)\Phi_k^n\left(u^2\right)\vec{r}_{j,k} \tag{12}$$

where the interpolation polynomials are expressed as:

$$\Phi_i^n\left(u\right)=R_i(n,u)R_{n-i}(n,1-u) \tag{13}$$

where $R_i(n,u)$ is a Sylvester interpolation polynomial [16]:

$$R_i(n,u)=\begin{cases}\dfrac{1}{i!}\displaystyle\prod_{k=0}^{i-1}\left(nu-k\right), & 1\le i<n\\ 1, & i=0\end{cases} \tag{14}$$

It is noted that this interpolation procedure exactly represents a bi-linear quadrilateral when $n=1$, bi-quadratic quadrilateral when $n=2$, and a bi-cubic quadrilateral when $n=3$. It also represents interpolations to arbitrary order.

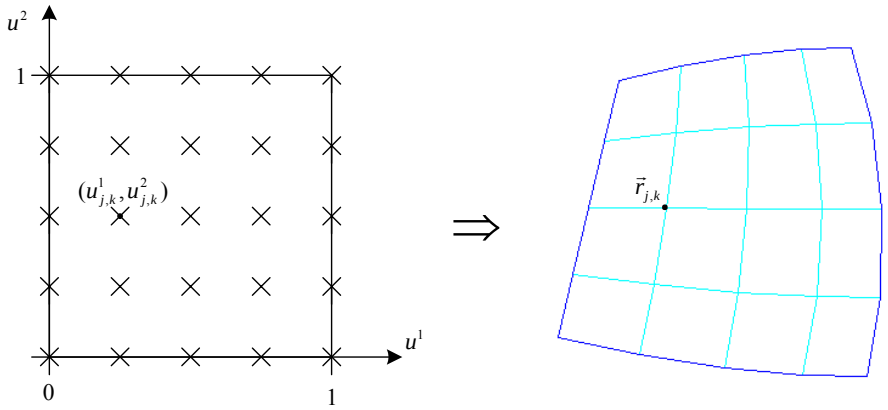

Fig. 2. Mapping of a fourth-order quadrilateral cell from the unitary space to the physical patch.

The unitary vectors for the patch are then computed as:

$$\vec{a}_i = \frac{\partial \vec{r}(u^1,u^2)}{\partial u^i} = \frac{\partial}{\partial u^i}\sum_{k=0}^{n}\sum_{j=0}^{n}\Phi_j^n\left(u^1\right)\Phi_k^n\left(u^2\right)\vec{r}_{j,k} \tag{15}$$

Analytical expressions for the derivatives of the interpolation polynomials are easily derived, and the derivatives of the Sylvester interpolation polynomials can be expressed via a recursive relationship that is efficiently computed.

This scheme is general enough to interpolate surfaces up to arbitrary order. However, it still must be realized that the interpolation scheme is only C^0 continuous. And, for very high-orders ($\sim n > 10$) the interpolation operator can be ill conditioned. As a result, Gibb's phenomena can occur leading to small high spatial-frequency oscillation of the interpolated surface. These issues can be resolved by working with interpolation functions that enforce higher degrees of continuity across patch boundaries (e.g., splines or NURBS) and possibly using non-uniform point sampling that minimizes the determinant of the Vandermonde matrix (e.g., Lobatto or Chebyshev point sampling). Nevertheless, the interpolation scheme proposed in (12) works quite well to reasonably high order.

In a general implementation of a method of moment code, one would like to use an object-oriented approach such that kernel evaluations are essentially independent of the patch type or order. That is, one would like to use the same code for bi-linear quads, high-order quads, or specific curvilinear patches that exactly conform to a canonical surface (e.g., spherical, conical, cylindrical, or ellipsoidal surfaces). This is easily done by defining a class (or a function) that simply returns the position vector and the unitary vectors given the local curvilinear coordinates (u^1,u^2) for the source or field patch. In this way, the kernel of the code has no direct dependencies on the source or field patch types.

V. Numerical Integration Issues

The operators defined in (4)-(10) require the computation of a convolutional integral performed over an arbitrary "source" patch and computed to a field point. This convolution is estimated using numerical integration. How this integration is computed will depend upon the separation of the field quadrature point and the source patch and the level of accuracy desired. If the field point lies on the source patch, then the kernel is singular and must be treated specially. If the field point is close to the source patch, then the integration must be performed using some

type of adaptive numerical quadrature. In general, if *d* digits of accuracy is expected from the final solution, then *d*-digits of accuracy should be demanded from the adaptive quadrature routine. This defines the "near" region. Adaptive quadrature is not needed once the field point is sufficiently far away that the fixed-point quadrature rule of the Nyström discretization provides at least *d*-digits of accuracy. This defines the "far" region. In the near region, adaptive quadrature is used to compute the convolutional integral to *d*-digits of accuracy. Then, a local correction is performed that effectively maps the current coefficient vector to the currents at the quadrature points (c.f., Sections II and III, pp. 2402-2404 of [2]). In the far region this leads to the single point-to-point reaction that is equivalent to estimating the numerical integration of the convolutional integral with a fixed-point quadrature rule.

The most difficult integration to perform in the near region is the singular integrations. The **L** operator has a hypersingularity and must be properly manipulated so that it is numerically tractable. The **K** operator has an integrable $1/R$ singularity. However, care still must be taken to compute this in an efficient manner.

Initially, consider the treatment of the **L** operator. Specifically, from (6)

$$\vec{t}_m \cdot \mathbf{L}_i\left(\vec{J}_n\right) = -jk_i\left[\vec{t}_m \cdot \int_{S'} \vec{J}_n(\vec{r}')G_i(\vec{r}_m,\vec{r}')ds' + k_i^{-2}\vec{t}_m \cdot \nabla\int_{S'}\left(\nabla G_i(\vec{r}_m,\vec{r}')\cdot\vec{J}_n(\vec{r}')\right)ds'\right] \tag{16}$$

where, $\vec{J}_n(\vec{r}')$ is the vector basis function in (11), $\vec{r}_m$ is an abscissa point of the quadrature rule on the field patch, and the test vector $\vec{t}_m$ is evaluated at $\vec{r}_m$. The integrand of the first integral in (16) has a $1/R$ singularity. However, due to the double ∇ operator, the integrand of the second integral is hypersingular in the limit $R \to 0$. In fact, it exhibits a singularity of $\mathcal{O}\left(1/R^3\right)$. Consequently, this term must be manipulated to reduce the order of singularity. Thus, we will focus on manipulating this term. Initially, the following identity can be derived:

$$\begin{aligned}\int_S \vec{t}_m \cdot \nabla\left(\left(\nabla G_i(\vec{r}_m,\vec{r}')\right)\cdot\vec{J}_n(\vec{r}')\right)ds' &= -\int_S\left(\vec{t}_m\cdot\nabla\right)\left(\vec{J}_n(\vec{r}')\cdot\nabla'_{\|}\right)\left(G_i(\vec{r}_m,\vec{r}')\right)ds' \\ &= -\int_S\left(\vec{J}_n(\vec{r}')\cdot\nabla'_{\|}\right)\left(\vec{t}_m\cdot\nabla\right)\left(G_i(\vec{r}_m,\vec{r}')\right)ds',\end{aligned} \tag{17}$$

where we have made use of the reciprocal nature of the Green function such that $\nabla G_i(\vec{r}_m,\vec{r}') = -\nabla' G_i(\vec{r}_m,\vec{r}')$ and the complimentary nature of the operators $\left(\vec{J}_n(\vec{r}')\cdot\nabla'_{\|}\right)\left(\vec{t}_m\cdot\nabla\right)$. Also, $\nabla'_{\|}$ is the projection of the gradient operator onto the surface tangent. Next, utilizing a vector identity, the right-hand-side of (17) is rewritten as

$$= -\int_S \nabla'_{\|}\cdot\left[\vec{J}_n(\vec{r}')\left(\vec{t}_m\cdot\nabla G_i(\vec{r}_m,\vec{r}')\right)\right]ds' + \int_S \nabla'_{\|}\cdot\vec{J}_n(\vec{r}')\left(\vec{t}_m\cdot\nabla G_i(\vec{r}_m,\vec{r}')\right)ds'. \tag{18}$$

The first term on the right-hand-side of (18) can be rewritten using the divergence theorem for open surfaces [1] as:

$$-\int_S \nabla'_{\|}\cdot\left[\vec{J}_n(\vec{r}')\left(\vec{t}_m\cdot\nabla G_i(\vec{r}_m,\vec{r}')\right)\right]ds' = -\oint_C\left(\hat{e}'\cdot\vec{J}_n(\vec{r}')\right)\left(\vec{t}_m\cdot\nabla G_i(\vec{r}_m,\vec{r}')\right)dl' \tag{19}$$

where C is the closed contour bounding the open surface S, and $\hat{e}'$ is the outward normal to the contour that is also tangential to the surface (i.e., $\hat{e}'dl' = d\vec{l}' \times \hat{a}_n$, where $\hat{a}_n$ is the outward normal to S). Next, the second-term on the right-hand-side of (18) is rewritten as:

$$\int_S \left(\nabla'_{\parallel} \cdot \vec{J}_n(\vec{r}')\right)\left(\vec{t}_m \cdot \nabla G_i(\vec{r}_m, \vec{r}')\right) ds' = \int_S \nabla G_i(\vec{r}_m, \vec{r}') \cdot \left[\vec{t}_m \nabla'_{\parallel} \cdot \vec{J}_n(\vec{r}')\right] ds' \tag{20}$$

This term still has a singularity which is $\mathcal{O}\left(1/R^2\right)$. To reduce this by one order, the right-hand-side of (20) is rewritten as:

$$= \int_S \nabla G_i(\vec{r}_m, \vec{r}') \cdot \left[\vec{t}_m \nabla'_{\parallel} \cdot \vec{J}_n(\vec{r}') - \vec{K}_{mn}\left(\vec{r}'\right)\right] ds' + \int_S \nabla G_i(\vec{r}_m, \vec{r}') \cdot \vec{K}_{mn}\left(\vec{r}'\right) ds' \tag{21}$$

where, $\vec{K}_{m,n}\left(\vec{r}'\right)$ is defined by

$$\vec{K}_{mn}\left(\vec{r}'\right) = \frac{\vec{\Psi}_m\left(\vec{r}'\right)}{\sqrt{g'}} \chi_{n,m}, \tag{22}$$

where $\chi_{n,m}$ is the constant:

$$\chi_{n,m} = \left(\sqrt{g} \nabla'_{\parallel} \cdot \vec{J}_n(\vec{r}')\right)\Big|_{\vec{r}' = \vec{r}_m}, \tag{23}$$

and the vector $\vec{\Psi}_m\left(\vec{r}'\right)$ is defined by:

$$\vec{\Psi}_m\left(\vec{r}'\right) = \left(\vec{t}_m \cdot \vec{a}^1\right)\Big|_{\vec{r}' = \vec{r}_m} \vec{a}_1\left(\vec{r}'\right) + \left(\vec{t}_m \cdot \vec{a}^2\right)\Big|_{\vec{r}' = \vec{r}_m} \vec{a}_2\left(\vec{r}'\right) \tag{24}$$

such that at the singular point $\vec{K}_{mn}\left(\vec{r}_m\right) = \vec{t}_m \nabla'_{\parallel} \cdot \vec{J}_n(\vec{r}')\Big|_{\vec{r}' = \vec{r}_m}$. Consequently, the singularity in the first term on the right-hand side of (21) is simply $\mathcal{O}\left(1/R\right)$ and is numerically tractable. The second term in (21) can be simplified to:

$$\begin{aligned} \int_S \nabla G_i(\vec{r}_m, \vec{r}') \cdot \vec{K}_{mn}\left(\vec{r}'\right) ds' &= -\int_S \left[\nabla'_{\parallel} \cdot \left(\vec{K}_{mn}\left(\vec{r}'\right) G_i(\vec{r}_m, \vec{r}')\right) - G_i(\vec{r}_m, \vec{r}') \nabla'_{\parallel} \cdot \vec{K}_{mn}\left(\vec{r}'\right)\right] ds' \\ &= -\oint_C \hat{e}' \cdot \vec{K}_{mn}\left(\vec{r}'\right) G^R(\vec{r}_m, \vec{r}') dl' \end{aligned} \tag{25}$$

However, from (22)-(24), it is immediately seen that $\nabla'_{\parallel} \cdot \vec{K}_{m,n}\left(\vec{r}'\right) = 0$. Then, applying the open surface divergence theorem on the remaining term:

In summary, from (17)-(25):

$$\begin{aligned} \vec{t}_m \cdot \nabla \int_S \left(\nabla G_i(\vec{r}_m, \vec{r}') \cdot \vec{J}(\vec{r}')\right) ds' &= + \int_S \nabla G_i(\vec{r}_m, \vec{r}') \cdot \left[\vec{t}_m \nabla'_{\parallel} \cdot \vec{J}(\vec{r}') - \vec{K}_{mn}\left(\vec{r}'\right)\right] ds' \\ &\quad - \oint_C \left(\hat{e}' \cdot \vec{J}(\vec{r}')\right)\left(\vec{t}_m \cdot \nabla G_i(\vec{r}_m, \vec{r}')\right) dl' - \oint_C \hat{e}' \cdot \vec{K}_{mn}\left(\vec{r}'\right) G_i(\vec{r}_m, \vec{r}') dl'. \end{aligned} \tag{26}$$

It is assumed that the Nyström discretization points are interior to S and do not lie on the contour C. Consequently, the surface integration in (26) and the leading term in (16) have an integrable

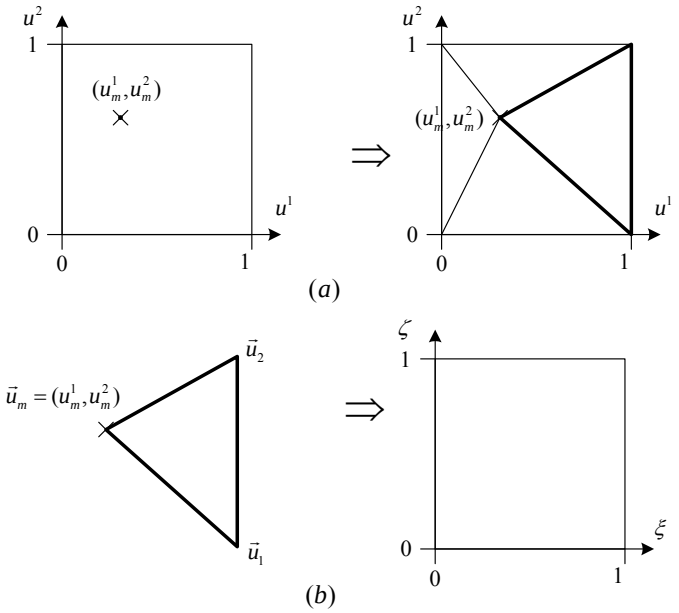

Fig. 3 (a) Decomposing the unitary square into triangles with common vertex at the singular point. (b) Mapping the "Duffy-triangle" into a parameter space.

$\mathcal{O}(1/R)$ singularity. Similarly, the surface integral arising from the **K**-operator is also $\mathcal{O}(1/R)$. These surface integrals can be computed efficiently and to controllable accuracy using a Duffy transformation [17] and adaptive numerical quadrature. The contour integrals are non-singular and can be computed directly using one-dimensional adaptive quadrature routines.

The Duffy Transform

At this point it deems instructive to review the integration of a singular integral via the Duffy transformation. Consider the integration over a quadrilateral cell:

$$I(\vec{r}_m) = \vec{t} \cdot \int_S \overline{\overline{K}}(\vec{r}_m, \vec{r}') \cdot \vec{J}(\vec{r}') ds' = \vec{t} \cdot \int_{u^2=0}^{1} \int_{u^1=0}^{1} \overline{\overline{K}}(\vec{r}_m, \vec{r}'(u^1, u^2)) \cdot \vec{J}(\vec{r}'(u^1, u^2)) \sqrt{g}\, du^1 du^2 \qquad (27)$$

where $\overline{\overline{K}}$ represents a dyadic kernel that has a $1/R$ singularity at $\vec{r}_m$ and it is assumed that $\vec{r}_m \in S$. Initially, the quadrilateral cell is triangulated with a set of triangles that share a common point at $\vec{r}_m$, which is defined by local unitary coordinates (u_m^1, u_m^2). This is depicted in the unitary space in Fig. 3 (a). The integration over the quadrilateral is then expressed as a superposition of the integration over each "Duffy triangle." Each Duffy triangle is then mapped into a parametric space as illustrated in Fig. 3 (b) such that the singular point is mapped to the edge $u = 0$. Thus,

$$I(\vec{r}_m) = \sum_{\ell=1}^{N_\Delta} \vec{t} \cdot 2A_\ell \int_{\zeta=0}^{1} \int_{\xi=0}^{1} \overline{\overline{K}}(\vec{r}_m, \vec{r}'(u^1, u^2)) \cdot \vec{J}(\vec{r}'(u^1, u^2)) \sqrt{g(u^1, u^2)}\, \xi\, d\xi d\zeta \qquad (28)$$

where N_Δ is the number of Duffy triangles, and A_ℓ is the area of the ℓ-th triangle (computed in the unitary space). From Fig. 3 (b):

$$2A_\ell = \left| (\vec{u}_1 - \vec{u}_m) \times (\vec{u}_2 - \vec{u}_m) \right|. \qquad (29)$$

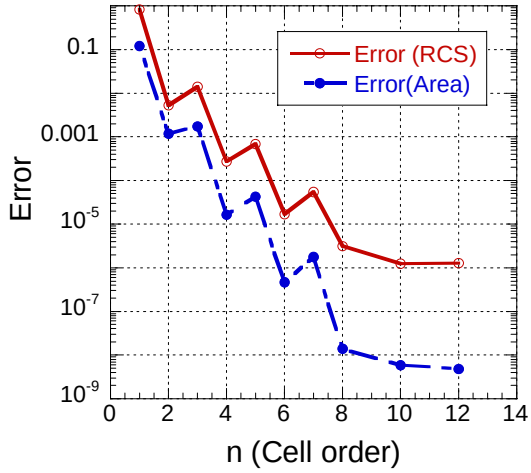

Fig. 4 Relative mean error in the RCS of a sphere of radius $k_o a = 6$ computed via the LCN method with ninth-order basis versus the interpolation order *n* of the 24 curvilinear cells. Also compared in the graph is the relative error of the area of the patched sphere.

There is also a simple linear mapping from the parametric coordinates to the unitary coordinates:

$$\vec{u} = \left(u^1, u^2\right) = \left(1-\xi\right)\vec{u}_m + \xi\left(1-\zeta\right)\vec{u}_1 + \xi\zeta\,\vec{u}_2 . \tag{30}$$

When evaluating (28), one first computes (u^1, u^2) from the parametric coordinates and then computes $\vec{r}'(u^1, u^2)$, the unitary vectors and $\sqrt{g}$. Though, it is worth noting that since the current basis functions in (11) normalized by $\sqrt{g}$, this term cancels in an actual implementation.

VI. Some Numerical Results

We have implemented the LCN solution for a number of integral operators and have reported the results in [2, 4, 10, 12, 14]. Additional studies have been reported in [1, 5, 18]. Here we present a few examples mainly to study the convergence characteristics of the LCN method. Initially, we will study the electromagnetic scattering by a PEC sphere of radius *a* defined by $k_o a = 6$. The sphere was discretized with 24 quadrilateral curvilinear cells as defined in Section IV. Initially, the basis function order was set to $p = 9$. Similarly, a 9×9-point Gauss-Legendre quadrature rule was used for the Nyström discretization of each patch. Thus, there are a total of 3,888 unknowns. Then, the order of the cells was increased from $n = 1$ to $n = 12$. The bistatic RCS was then computed for the sphere and the mean relative error was calculated relative to a Mie-series solution as:

$$\text{Mean Error} = \frac{1}{N_a}\sum_{i=1}^{N_a}\frac{\left|\sigma^{LCN}\left(\theta_i,\phi_i\right) - \sigma^{Mie}\left(\theta_i,\phi_i\right)\right|}{\left|\sigma^{Mie}\left(\theta_i,\phi_i\right)\right|} \tag{31}$$

where N_a is the number of angles (360 uniformly spaced angles were computed). A graph of the mean relative error versus the cell order *n* computed for the MFIE is illustrated in Fig. 4. The error in the area of the sphere as approximated via the 9×9-point Gauss-Legendre quadrature rule is also graphed in Fig. 4 as a comparison. Initially, it is observed that error in the RCS and the area follow the same general trend. It also appears that the minimum error is reached when

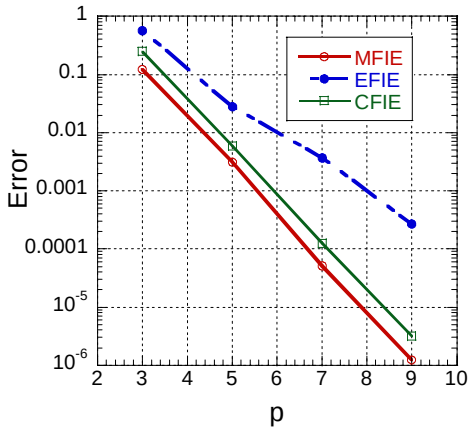

Fig. 5 Relative mean error in the RCS of a sphere of radius $k_o a = 6$ computed via the LCN method versus the basis order p.

$n = p+1$. It is also observed that even cell orders (which have an odd number of points) converge at a different rate than odd cell orders for an odd-order quadrature rule.

Next, the error in the RCS was computed for the sphere as a function of the basis order. In each case, the cell order is set so that $n = p+1$. The RCS was predicted via the MFIE ($\alpha = 0$ in (10)), the EFIE ($\alpha = 1$) and the CFIE ($\alpha = 0.1$), and the mean error was predicted via (31). A graph of the mean relative error versus order p is illustrated in Fig. 5 for p = 3, 5, 7, and 9. The MFIE is converging optimally with the error decreasing nearly two orders of magnitude as p is increased by 2 orders. The EFIE is converging at a slower rate, and the CFIE is somewhat in-between. It is also noted that the number of degrees of freedom for each case is equal to $24 \times 2p^2$, since there are 24 cells, p^2 basis and quadrature points, and 2 vector projects per quadrature point. Finally, Fig. 6 illustrates the bistatic RCS for p = 5 as compared to the Mie-series solution. There is no observable difference for the MFIE and CFIE solutions, and only a very slight discernable difference for the EFIE solution. These simulations required only 1200 unknowns. We should also point out that the average patch edge length is $\sim 0.75\lambda_o$. Thus, with p = 5, this corresponds to a discretization of < 7 unknowns per linear wavelength.

Finally, we illustrate the scattering by the EMCC metallic ogive [19]. The curvilinear cell discretization of the ogive is illustrated in Fig. 7 (288 cells n = 7). The ogive is 10 inches long along the major axis and has a 1 inch radius at the center. The monostatic RCS of the ogive at 9 GHz computed in the 0^o elevation plane ($\theta = 90^o$) is illustrated in Fig. 8. This was computed via the MFIE with p = 4. These results compare extremely well to the measured data and predictions by Cicero in Fig. 9, pg. 86 of [19]. At this frequency, the ogive is approximate 7.6 λ_o long and has a radius of 0.76 λ_o at the center. These results were obtained using only 9,216 unknowns.

Acknowledgements

This work has been sponsored by the DARPA VET program through grant MDA971-01-1-0022 and the Army Research Office through contract DAAD-19-99-1-0093 with the University of Kentucky. The authors would also like to acknowledge the Computational Physics Group at HRL Laboratories, Malibu CA, for their pioneering work on the LCN method.

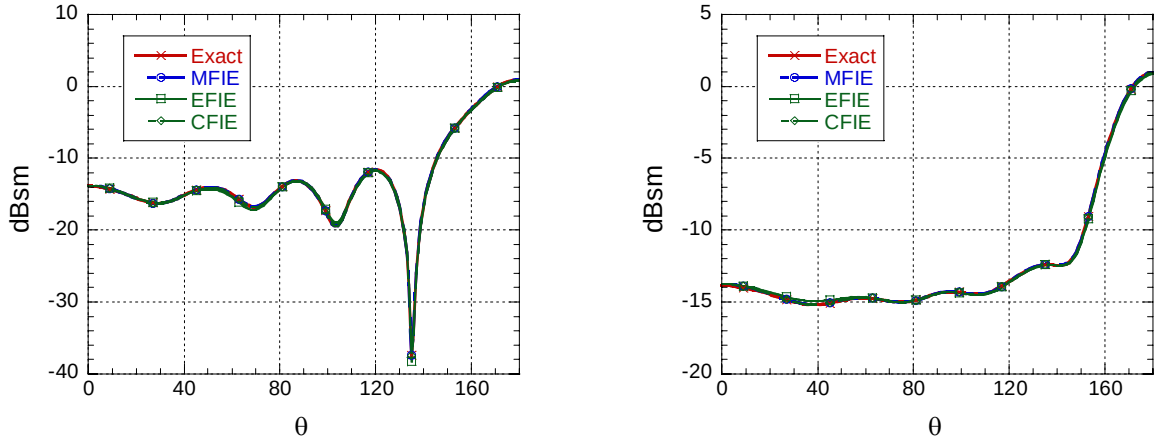

Fig. 6 Bistatic RCS of a sphere of radius $k_o a = 6$ computed via the LCN solution of the MFIE, EFIE, and CFIE compared to an exact Mie series solution (24 cells, $p = 5$, $n = 6$).

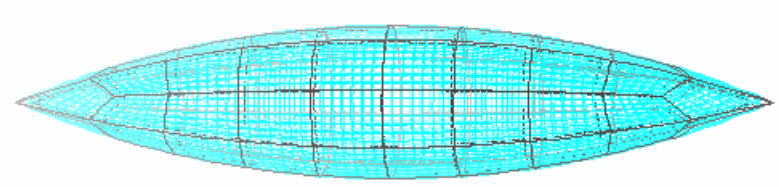

Fig. 7 The EMCC metallic ogive [19] approximated by 72 curvilinear cells ($n = 7$).

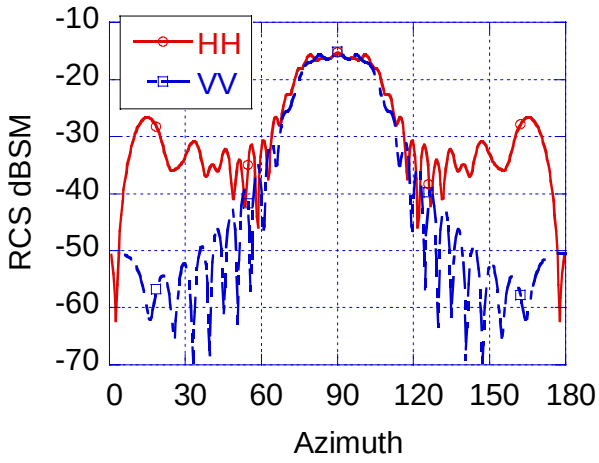

Fig. 6 Monostatic RCS of the EMCC metallic ogive at 9 GHz.

References

[1] L. F. Canino, J. J. Ottusch, M. A. Stalzer, J. L. Visher, and S. M. Wandzura, "Numerical solution of the Helmholtz equation in 2D and 3D using a high-order Nyström discretization," *Journal of Computational Physics*, vol. 146, pp. 627-663, 1998.

[2] S. D. Gedney, "On Deriving a Locally Corrected Nyström Scheme from a Quadrature Sampled Moment Method," *IEEE Transactions on Antennas and Propagation*, vol. 51, pp. 2402-2412, 2003.

[3] G. Liu and S. D. Gedney, "High-Order Moment Method Solution for the Scattering Analysis of Penetrable Bodies," *Electromagnetics*, vol. 23, 2003.

[4] S. D. Gedney and C. C. Lu, "High-Order Solution for the Electromagnetic Scattering by Inhomogeneous Dielectric Bodies," *Radio Science*, vol. 38, pp. 1015, 2003.

[5] A. F. Peterson, "Accuracy of currents produced by the Locally-corrected Nyström method and the Method of Moments when used with higher-order representations," *Applied Computational Electromagnetics Society Journal*, vol. 17, pp. 74-83, 2002.

[6] C. Müller, *Foundations of the Mathematical Theory of Electromagnetic Waves*, vol. 301. Berlin: Springer-Verlag, 1969.

[7] R. F. Harrington, "Boundary integral formulations for homogeneous material bodies," *Journal of Electromagnetic Waves and Applications*, vol. 3, pp. 1-15, 1989.

[8] X. Q. Sheng, J. M. Jin, J. M. Song, W. C. Chew, and C. C. Lu, "Solution of combined-field integral equation using multilevel fast multipole algorithm for scattering by homogeneous bodies," *IEEE Transactions on Antennas and Propagation*, vol. 46, pp. 1718-1726, 1998.

[9] A. F. Peterson, S. L. Ray, and R. Mittra, *Computational Methods for Electromagnetics*. New York: IEEE Press, 1998.

[10] S. D. Gedney, "High-Order Method of Moment Solution of the Scattering by Three-Dimensional PEC Bodies using Quadrature Based Point Matching," *Microwave and Optical Technology Letters*, vol. 29, pp. 303-309, 2001.

[11] J. A. Stratton, *Electromagnetic Theory*. New York: McGraw-Hill, 1941.

[12] S. D. Gedney, "Application of the High-Order Nyström Scheme to the Integral Equation Solution of Electromagnetic Interaction Problems," presented at IEEE International Symposium on Electromagnetic Compatibility, Washington, D.C., 2000.

[13] F. Çaliskan and A. F. Peterson, "The need for mixed-order representations with the locally corrected Nystrom method," *IEEE Antennas and Wireless Propagation Letters*, vol. 2, pp. 72- 73, 2003.

[14] S. D. Gedney, A. Zhu, and C. C. Lu, "Study of mixed-order basis functions for the locally-corrected Nyström method," *IEEE Transactions on Antennas and Propagation*, submitted, 2003.

[15] A. H. Stroud, *Approximate Calculation of Multiple Integrals*. Englewood Cliffs, NJ: Prentice-Hall, 1971.

[16] P. P. Silvester and R. L. Ferrari, *Finite Elements for Electrical Engineerings*, 2nd ed. Cambridge: Cambridge University Press, 1990.

[17] M. G. Duffy, "Quadrature over a pyramid or cube of integrands with a singularity at a vertex," *SIAM Journal on Numerical Analysis*, vol. 19, pp. 1260-1262, 1982.

[18] K. C. Donepudi, J. M. Jin, S. Velamparambil, J. M. Song, and W. C. Chew, "A higher order parallelized multilevel fast multipole algorithm for 3-D scattering," *IEEE Transactions on Antennas and Propagation*, vol. 49, pp. 1069-1078, 2001.

[19] A. C. Woo, H. T. G. Wang, and M. J. Schuh, "Benchmark radar targets for the validation of computational electromagnetics programs," *IEEE Antennas and Propagation Magazine*, vol. 35, pp. 84-89, 1993.